

Chapter 2

Infrared Vision: Visual Inspection Beyond the Visible Spectrum

Clemente Ibarra-Castanedo, Stefano Sfarra, Marc Genest
and Xavier Maldague

Abstract Infrared (IR) vision for the nondestructive testing (NDT) of materials has considerably grown in the last few years as a results of the continual technological progress and the development of advanced signal processing techniques. Typical applications can be divided into two groups: (1) reflectography/transmittography in the near (NIR) and short-wave (SWIR) infrared spectra, which have been recently applied in the inspection of semitransparent composite materials such as glass, aramid–phenolic, and a variety of natural fibers; and (2) infrared thermography, which involves the detection of surface and subsurface defects based on the differences in thermal signatures in the mid-wave (MWIR) and long-wave (LWIR) infrared bands. Infrared reflectography and thermography have shown interesting complementarities between them as well as with other NDT methods such as ultrasound testing, eddy current testing, and holographic interferometry. In this chapter, a review of classical and recent applications of infrared vision is provided and discussed in detail with examples.

C. Ibarra-Castanedo (✉) · X. Maldague
Computer Vision and Systems Laboratory, Université Laval, 1065, av. de la Médecine,
Quebec G1V 0A6, Canada
e-mail: IbarraC@gel.ulaval.ca

X. Maldague
e-mail: MaldagX@gel.ulaval.ca

S. Sfarra
Las.E.R. Laboratory, Department of Industrial and Information Engineering and Economics
(DIIE), University of L'Aquila, Piazzale E. Pontieri no. 1, 67100 Monteluco di Roio—
L'Aquila, AQ, Italy
e-mail: Stefano.Sfarra@univaq.it

M. Genest
National Research Council Canada, 1200 Montreal Road, Bldg. M-14, Room 130, Ottawa,
ON K1A 0R6, Canada
e-mail: Marc.Genest@nrc-cnrc.gc.ca

Contents

2.1 Infrared Vision 42

2.2 NonThermal Infrared Vision 44

2.3 Thermal Infrared Vision 44

2.4 Advanced Signal Processing 48

2.5 Experimental Configuration..... 48

2.6 Integrated Imaging Applications 49

 2.6.1 Inspection of Aramid–Phenolic Composites by Near
 Infrared Reflectography/Transmittography 49

 2.6.2 Integrated Infrared Vision Inspection of Jute and Hemp Fibers 50

 2.6.3 Assessment of Pultruded Kenaf/Glass Hybrid Composites 51

 2.6.4 Impacted Glass and Basalt Fiber Woven Composites 54

 2.6.5 Integrated Inspection of Jute Cloth/Wool Felts Hybrid Laminates 55

2.7 Conclusions 57

References 57

2.1 Infrared Vision

Infrared (IR) vision can be defined as a subdivision of computer vision, i.e., the use of computers to emulate human vision [1], which employs low-, mid-, and high-level computerized processes to analyze images generated in the infrared part of the electromagnetic (EM) spectrum. To “analyze images” is a very wide concept, which depends on the user’s goal (noise reduction, contrast enhancement, segmentation, etc.) as well as on the way images are generated (a single image, a dynamic sequence, etc.).

The EM spectrum, as depicted in Fig. 2.1, covers all kind of EM radiation, from γ -rays in the shortest wavelengths (in the order of femtometers, e.g., the size of the diameter of a gold nucleus ~ 8.45 fm) end of the spectrum (Fig. 2.1, left), to radio frequencies in the longest (in the order of megameters, e.g, the size of the Earth’s equatorial diameter ~ 12.7 Mm) wavelengths (Fig. 2.1, right).

The IR band is located between the visible (VIS) and the microwave spectra and can be subdivided using different definitions depending on the field of application. Figure 2.1 and Table 2.1 propose one of such classifications based on the atmosphere high-transmission windows as well as the type of detector materials that are sensible on each particular band. Four IR spectral bands are of interest for infrared vision applications: (1) the near infrared (NIR, from ~ 0.7 to $1\text{ }\mu\text{m}$), (2) the short-wave IR (SWIR, from ~ 1 to $2.5\text{ }\mu\text{m}$), (3) the mid-wave infrared (MWIR, from ~ 3 to $5\text{ }\mu\text{m}$), and (4) the long-wave infrared (LWIR, from ~ 7.5 to $14\text{ }\mu\text{m}$).

Strictly speaking, the terahertz region, which is between 100 and $1000\text{ }\mu\text{m}$ ($0.3\text{--}30\text{ THz}$), is part of the very long-wave infrared (VLWIR, from 14 to $1000\text{ }\mu\text{m}$). However, terahertz radiation can be considered as a special case of thermal infrared radiation, sharing some properties with the infrared and others from the microwave bands.

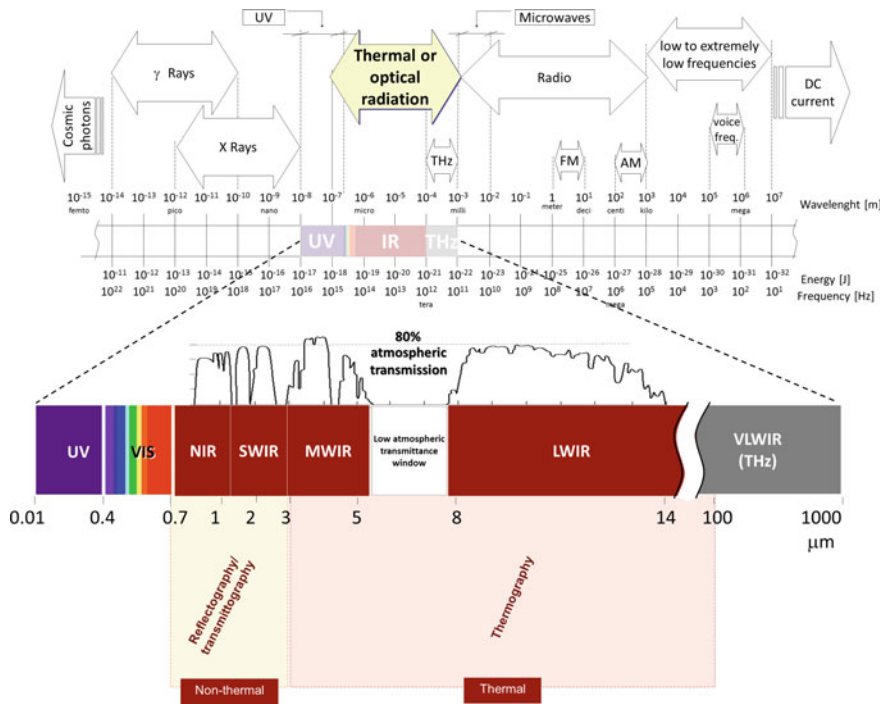


Fig. 2.1 The infrared bands in the electromagnetic spectrum

Table 2.1 Infrared spectral bands and the corresponding typical sensor materials [2, 3]

	Spectral band			Typical sensor materials
Nonthermal	NIR	Near infrared	0.7–1 μm	Si (0.5–1.1 μm)
				InGaAs (0.8–1.8 μm)
	SWIR	Short-wave infrared	1–2.5 μm	PbS (1.3–3.5 μm)
Thermal	MWIR	Mid-wave infrared	3–5 μm	InGaAs (0.8–1.8 μm)
				InAs (1–3.8 μm)
				HgCdTe (2–14 μm)
	LWIR	Long-wave infrared	7.5–14 μm	Microbolometers (amorphous silicon, vanadium oxide, etc.)
				HgCdTe (2–14 μm)

An additional and important distinction can be made between the spectral bands presented in Fig. 2.1 and Table 2.1. On the one hand, radiation from the NIR/SWIR spectra is the result of reflections from objects, which is similar to radiations in the visible spectrum, i.e., light, although NIR/SWIR light is not visible to humans, and can be considered as a nonthermal form of infrared radiation. On the other hand,

radiation from the MWIR/LWIR bands originates from the object's surface thermal emissions, and not reflections. These differences between IR bands give rise to a second subdivision of the IR spectrum into two groups: nonthermal and thermal.

2.2 NonThermal Infrared Vision

Nonthermal infrared vision is based on the detection of NIR or SWIR radiation reflected from (reflectography) or transmitted through (transmittography) the object of interest. Infrared reflectography and transmittography are based on the fact that, when an object is exposed to electromagnetic radiation, part of this radiation is reflected from the object surface, one part is transmitted through the object, and another is absorbed by the object. Radiation from the NIR and SWIR bands can thus penetrate some materials and be reflected by others.

This is illustrated in Fig. 2.2 for a semitransparent object without defects (top) and with an internal defect (bottom). The object is irradiated (I) from the left side, and as can be observed, part of the radiation passes through the object, another part is reflected, and another is absorbed. In the case of an object with an internal defect, opaque to this kind of radiation, part of the radiation that passes through the semitransparent material will be absorbed and reflected from (but not transmitted through) the defect. This will be revealed in the front (reflectography) and back (transmittography) surfaces of the object.

Proper selection of a continuous and uniform active illumination source is a critical part of a nonthermal inspection system. For instance, incandescent lamps provide a wide electromagnetic spectrum, going from the ultraviolet to the VLWIR (see Fig. 2.1 for reference). Fortunately, a vast part of the radiation from such a source is in the visible and the NIR and SWIR spectral bands, and therefore, it can be used as an illumination source. On the contrary, the EM spectrum of fluorescent lamps is narrower and with only a few distinctive high-intensity peaks mostly in the visible spectrum. Radiation emitted by this kind of lamps in the NIR/SWIR spectra is very limited and can hardly be used as a reliable illumination source. Light-emitting diodes (LEDs) are an example of a very interesting illumination source since they provide a narrow IR spectrum around specific wavelengths, from UV to VLWIR including the NIR and SWIR bands. The radiation source can be combined with the utilization of narrowband filters to further improve contrast [4].

2.3 Thermal Infrared Vision

Thermal infrared vision, also known as infrared thermography [5], is based on the utilization of a MWIR or LWIR infrared sensors, such as infrared cameras, to acquire thermal images or *thermograms*, from the surface of the object being observed. This can be performed in an *active* or a *passive* manner, i.e., with or

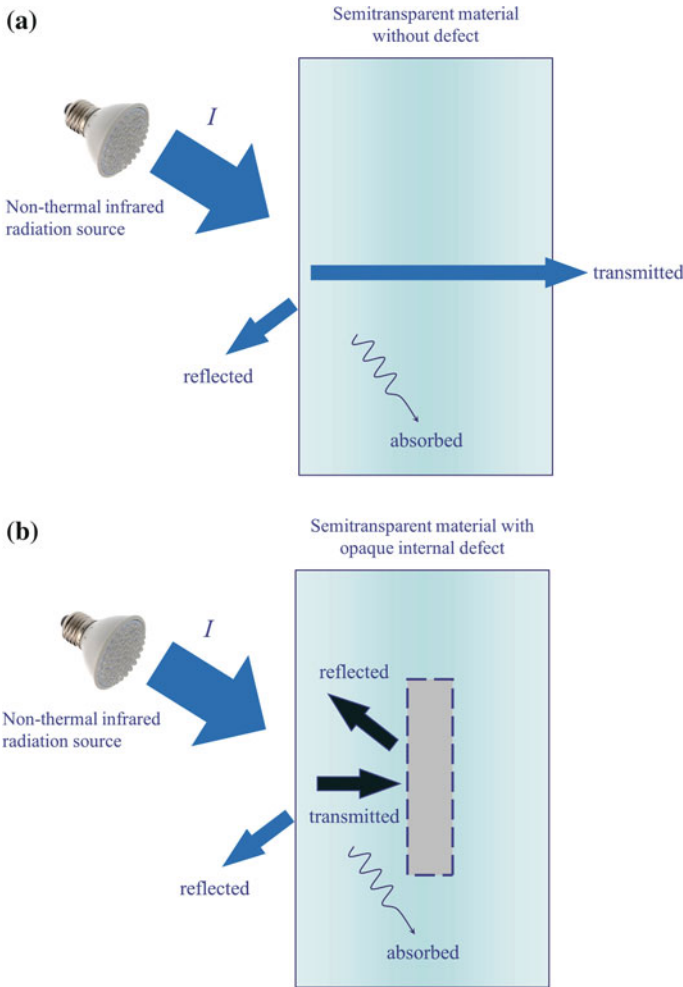


Fig. 2.2 Basic principle behind infrared reflectography/transmittography: semitransparent material exposed to nonthermal infrared radiation **a** without defect. **b** with opaque internal defect

without using an external heating (or cooling) source to promote a thermal contrast between dissimilar materials. In general, active thermography is of greater interest than passive thermography for the nondestructive evaluation (NDE) of materials, since an external thermal stimulation is normally required to disrupt the thermal equilibrium between defective and nondefective areas. Nonetheless, the passive approach has been successfully employed in a number of applications, e.g., aircraft inspection right after landing for water ingress assessment. Active infrared thermography is a well-established NDE technique [5, 6] that allows a fast inspection of large surfaces and is gaining popularity for the inspection of materials.

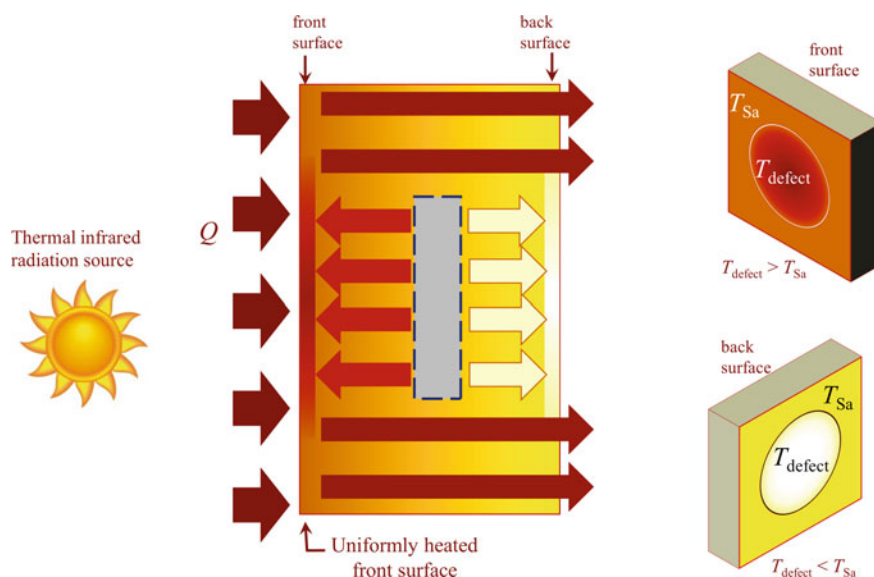


Fig. 2.3 Basic principle behind infrared thermography for an object with an internal defect acting as a thermal resistance

The basic principle behind active infrared thermography is depicted in Fig. 2.3, which illustrates the differences in heat propagation between areas with and without defect, for the case of a square specimen with an internal circular defect. Heat is uniformly applied to the left side surface, after which it propagates through the material by conduction. The heat front is uniformly distributed in the absence of internal defects. On the contrary, if an internal defect is present, it acts as a resistance to heat propagation. This is reflected in both the front and the back surfaces. In this example, it is assumed that the defect acts as a thermal resistance to heat. The situation would be different (the opposite) for the case of a defect acting as a heat sink.

Contrary to infrared reflectography/transmittography, where usually a single image is acquired and processed (after carefully selecting the appropriate illumination source and/or narrowband filters), infrared thermography for NDT applications requires the acquisition of a sequence of thermograms that are processed in time and space.

Several active thermography techniques have been proposed using specific scenarios adapted to particular applications. It is customary to categorize techniques according to the type of energy source and the waveform being employed. For instance, the energy source is commonly classified as follows[5–11]: optical, using either photographic flashes, halogen lamps, infrared lamps, lasers, or any other heat source based on the light emission process; ultrasound [12–14], in which a high-frequency sonic or ultrasonic source (typically 15–40 kHz) is applied to the sample; and inductive [15, 16], based on the principle of heat generation through

eddy currents. On the other hand, the energy delivered to the object can be of different forms: a pulse (few milliseconds), a square pulse or a step (several seconds or minutes), an amplitude and/or frequency modulated wave, or a dynamic scan (point, line, or surface).

Table 2.2 presents a summary of some of the most common active thermography configurations and their designations. According to Table 2.2, an experiment carried out using photographic flashes (short pulse) can be referred as optical pulsed thermography, while the inspection of a part using modulated ultrasounds would be known as ultrasound lock-in thermography.

Table 2.2 Active thermography common technique designations based on the type of energy source and the employed waveform

Source type	Waveform	Technique	Alternative designations
Optical	Short pulse	Optical pulsed thermography	Pulsed thermography (PT)
			Time-resolved thermography (TRIRT)
			Flash thermography
	Long pulse	Optical square pulsed thermography	Square pulsed thermography (SPT)
			Long pulsed thermography
	Step	Optical step heating thermography	Step heating thermography (SHT)
	Amplitude modulated	Optical lock-in thermography	Modulated thermography
Ultrasound	Frequency modulated	Optical chirp thermography	Frequency modulated thermography
	Line scan	Optical line scan thermography	Line scan thermography
Inductive	Burst	Ultrasound burst thermography	Vibrothermography (VT)
			Thermosonics
	Amplitude modulated	Ultrasound lock-in thermography	Lock-in vibrothermography
	Burst	Inductive burst thermography	Eddy current thermography (ECT)
			Pulsed eddy current thermography
	Amplitude modulated	Inductive lock-in thermography	Lock-in eddy current thermography
	Line scan	Inductive line scan thermography	–

2.4 Advanced Signal Processing

Typically, the acquired infrared data are processed to improve defect contrast and signal-to-noise ratio. Several processing techniques exist [5, 11, 17–19], from a basic cold image subtraction to more advanced techniques such as partial least squares thermography (PLST) [17].

The most relevant to the examples presented further are as follows: principal component thermography (PCT) [18], which reorganizes data into new components that take into account the main spatiotemporal variances of the sequence; and higher order statistics thermography (HOST) [19], which calculates the higher order centralized moments (3rd or skewness, 4th or kurtosis, or n th order moment) of the temporal temperature profiles summarizing all the relevant information about the original sequence into a single image.

In addition, in the reflectographic field, the image subtraction between the reflectogram and transmittogram acquired on the same specimen has been previously introduced [20]. The method intensifies the structure of the internal texture of semitransparent materials and shows with a good contrast the damage that has been produced by an impact loading.

For simplicity, only a brief review of the techniques has been provided. More details can be consulted in the provided references.

2.5 Experimental Configuration

The experimental configuration for nonthermal and thermal infrared vision is illustrated in Fig. 2.4. The radiation source ❶, thermal or nonthermal, is pointed toward the inspected object ❷ in either reflection (same side as the camera) or transmission (camera on the opposite side). The camera ❸ (NIR, SWIR, MWIR, or LWIR) records images from the object surface. The image acquisition and radiation sources are synchronized and controlled by a computer or control card ❹. Data (single images or sequences of several images) are stored and processed with a computer ❺.

Figure 2.4 is a schematic of the IR vision experimental setup using an optical source, i.e., an incandescent light bulb, which delivers wide-spectrum IR radiation covering both nonthermal and thermal applications. In practice, the illumination or heat sources are carefully selected depending on the application.

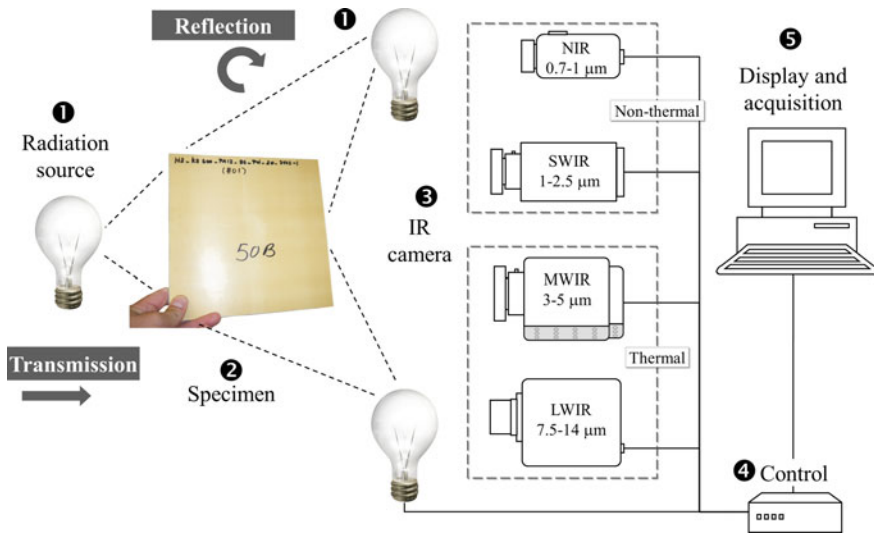


Fig. 2.4 Typical experimental setup for infrared vision

2.6 Integrated Imaging Applications

2.6.1 Inspection of Aramid–Phenolic Composites by Near Infrared Reflectography/Transmittography

The use of NIR reflectography/transmittography has shown to be very promising for the assessment of composite materials' semitransparent in the NIR/SWIR spectra [21]. For instance, Fig. 2.5 presents some results from an aramid–phenolic composite impacted specimen inspected from both sides in reflection and transmission modes. The top row corresponds to the front face and the bottom row to the back face of the specimen.

Photographs in Fig. 2.5a show the front (top) and back (bottom) views of the specimen. Some subtle indications of the impact can be observed in the close-up views in Fig. 2.5b, corresponding to approximately the area delimited by the black rectangle in Fig. 2.5a. The SWIR reflectograms presented in Fig. 2.5c show more details about the damage caused by the impact in both faces. Among other things, the specimen presents folds in three cardinal points around the impact (north, east, and west) as observed from the front face reflectogram (Fig. 2.5c, top). The back face reflectogram (Fig. 2.5c, bottom) only shows a fold north of the impact. However, contrary to front face inspection (Fig. 2.5c, top) where single fold is observed, the presence of two folds is evidenced in the back face inspection (Fig. 2.5c, bottom).

The transmittograms presented in Fig. 2.5d confirm the presence of the three folds visible from front face reflectogram (Fig. 2.5c, top) and apparently a fourth

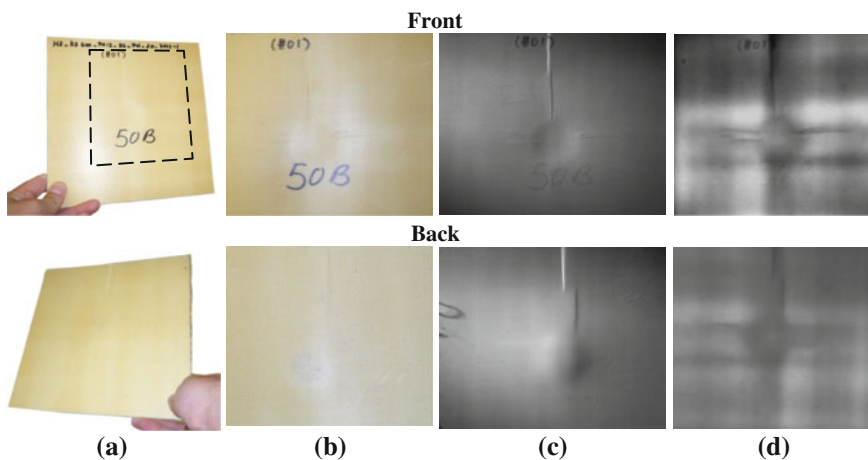


Fig. 2.5 Aramid-phenolic composite impacted specimen, front (*top row*) and back (*bottom row*) faces: **a** specimen photographs; **b** close-up views of the impacted area; **c** NIR reflectograms at 940 nm; and **d** NIR transmittograms at 780 nm

one south of the impact. Additionally, Fig. 2.5d provides information about the fibers and epoxy distribution inside the specimen. There are two bright stripes, one north and one south of the impact, indicating that fiber content is lesser in these areas, probably as a consequence of the impact that forced the fiber in the vertical and horizontal to congregate at the center of the impact.

2.6.2 Integrated Infrared Vision Inspection of Jute and Hemp Fibers

An example showing the complementarity of infrared transmittography and infrared thermography is presented in Fig. 2.6. These images correspond to a natural fiber composite specimen manufactured using six inner layers of jute plain weave disposed at $0^\circ/0^\circ/45^\circ/-45^\circ/0^\circ/0^\circ$ sandwiched between two nonwoven hemp mats. The laminate in this example has been impacted with a force 2339 N. Figure 2.6a shows the front side and Fig. 2.6b the back side of the specimen.

The specimen was inspected from the back side (radiated from the front side) by NIR and SWIR transmittography, and the results are shown in Fig. 2.6c, d, respectively. It is possible to see the extent of the damage inside the sample as well as the fiber distribution in both cases, although with some differences in contrast.

The sample was also inspected by square pulsed thermography (SPT) [22], 4 min heating–9 min cooling, using one 500-W lamp positioned in reflection mode from the back side. Data were then processed by principal component thermography (PCT) [23]. The resulting images correspond to the empirical orthogonal

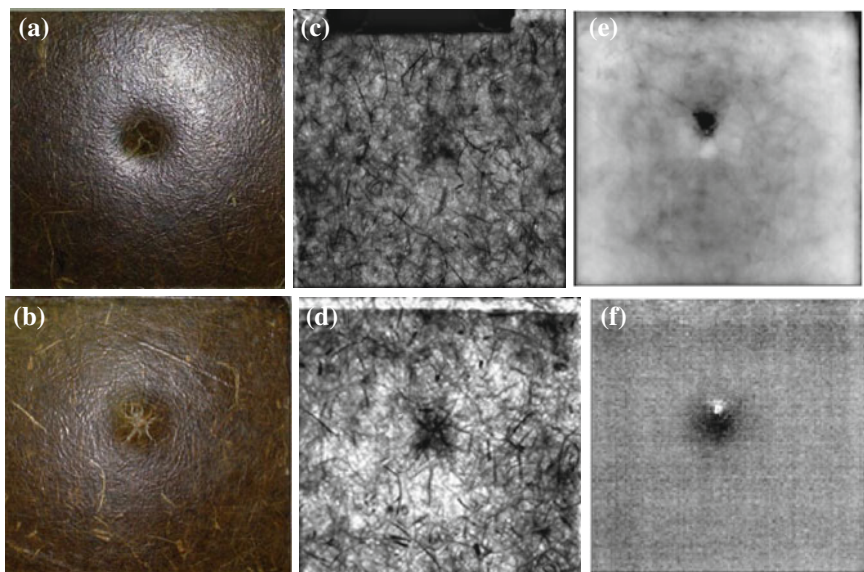


Fig. 2.6 **a** Front and **b** rear views of the specimen; **c** NIR (0.9–1.0 nm) transmittogram from the front face, **d** SWIR (1430 nm) transmittogram from the rear face; PCT results from square pulsed thermography (reflection from the front face): **e** EOF₃ and **f** EOF₁₂

functions (EOF), each one showing information at different depths. The EOF₃ in Fig. 2.6e is related to the damage close to the surface, while the EOF₁₂ in Fig. 2.6f corresponds to the damage deeper in the sample. As can be noted, the damaged area grows from the front to the back faces of the specimen: It is smaller in Fig. 2.6e than in Fig. 2.6f.

A similar specimen but impacted with considerably less force a maximum 1843 N is shown in Fig. 2.7.

Front and rear sides are reported in Fig. 2.7a, b, respectively. The transmittograms (Fig. 2.7c, d) show the presence of some areas at higher density of fibers highlighted with dark color, while the white color distinguishes the areas of low fiber density. Also in this case, the growth of the number linked to the EOF (from 4 to 14) indicates a growth of the depth explored starting from the face (Fig. 2.7e) to the rear side (Fig. 2.7f).

2.6.3 Assessment of Pultruded Kenaf/Glass Hybrid Composites

Another interesting case of semitransparent composite material is shown in Fig. 2.8. The specimen contains 40 kenaf + 25 glass as fiber content (wt%) and S/C/K/C/S as stacking sequence, with *S* = protection surface veil (made of 0.2 mm thickness

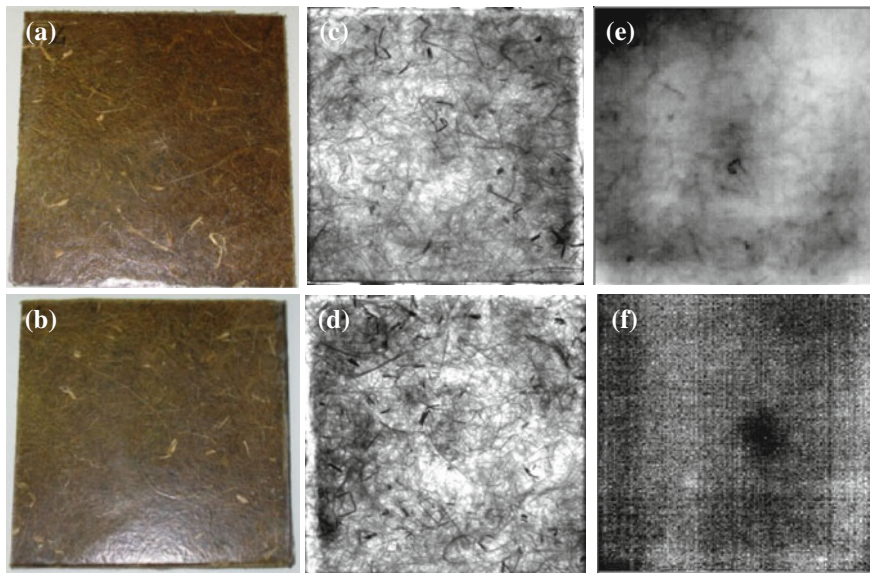


Fig. 2.7 **a** Front and **b** rear views of the specimen; **c** SWIR (1300 nm) transmittogram from the front face, **d** SWIR (1300 nm) transmittogram from the rear face; PCT results from square pulsed thermography (reflection from the front face): **e** EOF₄ and **f** EOF₁₄

polyester fibers); *C* = chopped strand mat (glass fibers); and *K* = kenaf fibers. The final dimensions were 140 mm x 22 mm x 2.8 (± 0.1) mm.

Indentation test was carried out by supporting the specimen on a steel plate with a 30 mm diameter circular opening, using a 10-mm-diameter hemispherical indenter as well as a 5584 universal testing machine (Instron) in displacement control with 1 mm/min crosshead speed [24].

As seen in Fig. 2.8, the internal structure of the composite is very different if compared to the external layer. The visible image in Fig. 2.8a shows a nonhomogeneous texture of the front side. For example, there is a horizontal rectangular area marked by an arrow that is also identifiable in the rear side (Fig. 2.8b). The energy applied in the indentation test has almost broken down the specimen (Fig. 2.8b—magnifications).

Comparing the reflectogram in Fig. 2.8c to the visible image of the same side (Fig. 2.8b), it is possible to notice that the described area disappears and the alignment of the external fibers is enhanced for the whole specimen.

Working in transmission mode (Fig. 2.8d), the specimen is discriminated like a radiograph, i.e., the areas having a higher concentration of fibers are distinguished from the others. However, a more in-depth study about this point is only possible by subtracting the reflectogram (Fig. 2.8c) to the transmittogram (Fig. 2.8d). Indeed, some areas classified at low concentration of fibers in the first approach are effectively more saturated at the end of the second step, as highlighted by the arrows in Fig. 2.8d, e.

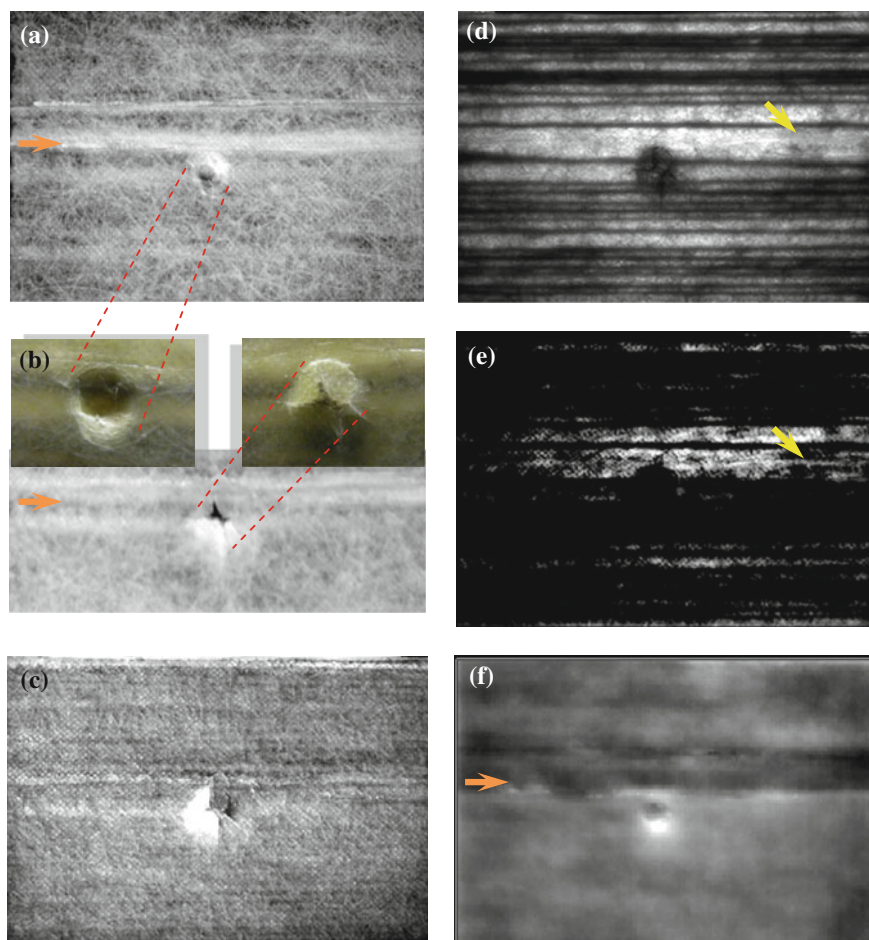


Fig. 2.8 **a** Front and **b** rear (close-up) views of the specimen and magnifications of the impact damages; **c** SWIR (940 nm) reflectogram from the rear face; **d** SWIR (940 nm) transmittogram from the rear face, **e** subtraction of images between **c** and **d**; PCT result from square pulsed thermography (reflection from the front face); and **f** EOF₃

Finally, the PCT result (EOF₃) presented in Fig. 2.8f reveals a horizontal rectangular area that has a larger extension compared to that identified by visual inspection in Fig. 2.8a, demonstrating the potential of thermography to identify subsurface features related with fiber distribution.

2.6.4 Impacted Glass and Basalt Fiber Woven Composites

Another example of integrated approach between visual inspection, SWIR, and thermographic techniques is presented in Fig. 2.9. The composite under inspection was produced by basalt fibers. The fiber volume fraction was equal to 0.38 ± 0.02 , and the thickness was approximately equal to 3 ± 0.1 mm [25]. Low-velocity impact test was conducted using a drop-weight impact tower fitted with an anti-rebound device. The impactor, with a 12.7 mm diameter, consists of a piezoelectric load cell to record the force and a high-speed video camera to record the impactor displacement during the impact test. Prior to undergoing impact loading, the sample was clamped to a square frame with a 73-mm square window. The mass of the bare impact carriage was 5 kg. The impact energy was equal to 15 J, and it was obtained by setting the impact height at 300 mm [26].

The front and the back sides of the specimen are shown in Fig. 2.9a, b, respectively. The damage caused by the impact is partially visible to the naked eye.

A very large detachment appears using SWIR when working in reflection mode, although at low contrast (Fig. 2.9c). The same defect can be fully detected in transmission mode by SWIR at 1050 nm (Fig. 2.9d); at the same time, the damage due to the impact loading can be revealed. In addition, the latter method enhances the visualization of a different texture of the fibers, compared to the surrounding area, where the dotted rectangle is positioned.

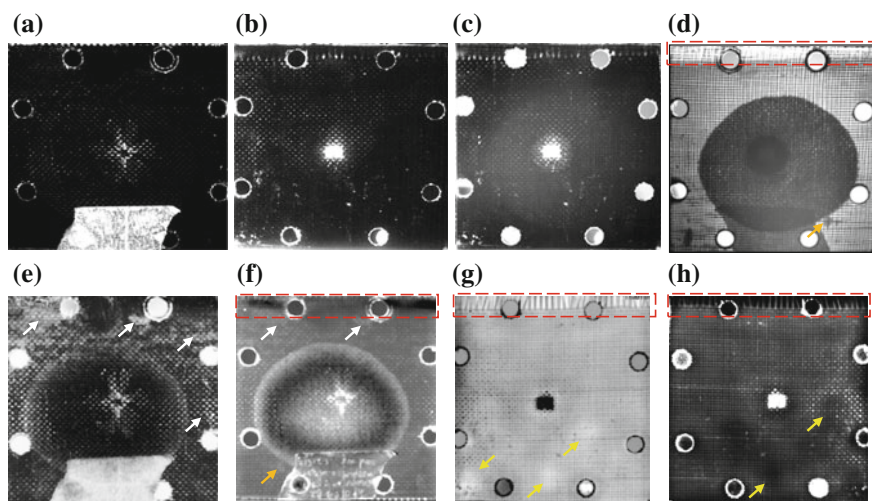


Fig. 2.9 **a** Front and **b** rear views of the specimen; **c** SWIR (1050 nm) reflectogram from the rear face, **d** SWIR (1050 nm) transmittogram from the back face; **e** HOST result (skewness) from pulsed thermography (reflection from the front face), **f** PCT result (EOF_4) from pulsed thermography (reflection from the front face), **g** PCT result (EOF_4) from pulsed thermography (reflection from the back face), and **h** HOST result (skewness) from pulsed thermography (reflection from the back face)

Some micro-detachments, pointed out by arrows, can be detected working in PT configuration and analyzing the IR data with HOST (skewness). Using this type of processing, the contour of the large detachment that surrounds the trace of the impact is still identifiable, while no thermal anomaly linked to statistical parameters reveals the presence of fiber misalignments at the north side of the specimen (Fig. 2.9e).

The latter defect is mapped by a dark color in Fig. 2.9f, by processing the IR data with PCT technique. In the same figure, some micro-detachments previously described are visualized and marked by arrows. One of these was already signaled in Fig. 2.9d by using an orange–brown arrow.

Additional anomalies are detected, identified by arrows in Fig. 2.9g, after inspecting the specimen from the back face, which also shows the texture of the fibers on the whole specimen. Finally, the detachments that are located below the large central detachment (Fig. 2.9g) are confirmed using HOST technique (skewness). The same consideration is valid for the fiber misalignments located along the north side of the specimen (Fig. 2.9h).

The large detachment around and above the impact could be due to poor adhesion between the resin and the fibers during sample fabrication.

2.6.5 *Integrated Inspection of Jute Cloth/Wool Felts Hybrid Laminates*

In Fig. 2.10 is shown a wool-based composite containing an amount of 40 vol.% (W-40) of wool fiber. From this laminate was cut the specimen. The specimen of dimensions $170 \text{ mm} \times 25 \text{ mm} \times 4 \text{ mm}$ ($L \times W \times t$) was subject to a low-velocity impact test using an in-house built drop-weight impact tower. The impactor diameter was 12.7 mm, and its mass was 1.25 kg, which was dropped from a height of 0.5 m, for an impact energy of approximately 6 J.

The specimen was produced by hand layup technique in a closed mold of dimensions $260 \times 160 \text{ mm}$ at room temperature using an epoxy resin (Mates SX10 ver.2 with hardener SX14). The laminate was cured under a slight pressure of 0.02 bars for 2 h, and then, it was removed from the mold and further cured at room temperature for at least 24 h before use [27].

The visual inspection of the front side (Fig. 2.10a) shows the damage produced by the impactor at the center of the specimen, while the rear side displays two dark areas. The first one, surrounded by an oval (Fig. 2.10b), is effectively larger than that visible to the naked eye. This assumption is confirmed in the near IR working in transmission mode (Fig. 2.10c) by using a metal-oxide semiconductor camera ($22.2 \times 14.8 \text{ mm}$, 10 MP, spectral band between 0.38 and $1.0 \mu\text{m}$), with a visible cutoff filter to limit the spectrum from 0.7 to $1.0 \mu\text{m}$.

The second one, surrounded by a square, can be seen with a good contrast in the near IR working in reflection mode (Fig. 2.10d).

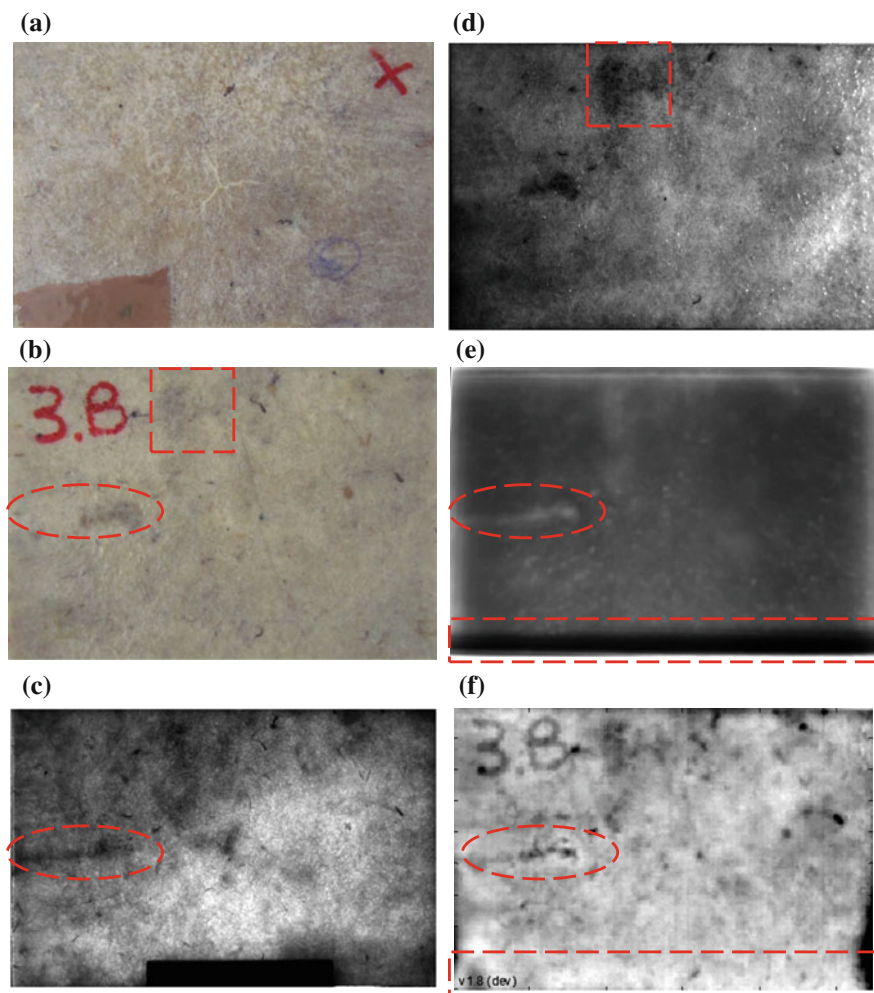


Fig. 2.10 **a** Front and **b** rear views of the specimen; **c** NIR (CMOS camera) transmittogram from the rear face, **d** NIR (CMOS camera) reflectogram from the rear face; **e** PCT result (EOF₂) from square pulsed thermography (reflection from the rear face), **f** PCT result (EOF₂) from pulsed thermography (reflection from the rear face)

In addition, the first anomaly (partially superficial and partially sub-superficial) is detected entirely by using square pulsed thermography (SPT) (Fig. 2.10e) and pulsed thermography (PT) (Fig. 2.10f).

PCT technique is able to reveal the presence of a horizontal rectangular area positioned along a border of the specimen, but with a reverse color, i.e., dark analyzing the SPT data (Fig. 2.10e) and white analyzing the PT data (Fig. 2.10f).

2.7 Conclusions

Infrared vision, thermal and nonthermal, is a very promising technique that is still finding new and interesting applications. NIR/SWIR reflectography/transmittography have shown a great potential for the inspection of semitransparent materials such as composites (glass, aramid–phenolic, or natural fibers). Active thermography is already widely used for the NDT of several materials. The observed complementarity between NIR/SWIR reflectography/transmittography and MWIR/LWIR thermography opens the door for integrated solutions for specific applications.

Acknowledgments Authors wish to thank Prof. Carlo Santulli, University of Camerino, Italy, for the loan of the composite natural fiber laminates used in this work and to the Canada Research Program (CRC): Multipolar Infrared Vision Canada Research Chair (MIVIM) for supporting part of this research.

References

1. Gonzalez RC, Woods RE, Eddins SL (2004) Digital image processing using MATLAB. Pearson Prentice Hall, Upper Saddle River, NJ
2. Rogalski A (2011) Recent progress in infrared detector technologies. *Infrared Phys Technol* 54:136–154
3. Rogalski A, Chrzanowski K (2002) Infrared devices and techniques. *Opto-Electron Rev* 10 (2):111–136
4. Ebeid A, Rott S, Talmy E, Ibarra-Castanedo C, Bendada A, Maldague X (2010) Near infrared imaging for multi-polar civilian applications. In: Proceedings of 10th International Conference on Quantitative InfraRed Thermography—QIRT, Quebec City, Canada, 27–30 July 2010
5. Maldague XP (2001) Theory and practice of infrared technology for nondestructive testing. Wiley, New York
6. Nondestructive Handbook. In: Maldague X, Moore PO Infrared and thermal testing, vol 3, 3rd edn. ASNT Press, Columbus, 718 p
7. Vollmer M, Möllmann K-P (2010) Infrared thermal imaging: fundamentals, research and applications. Wiley-VCH, Weinheim Germany
8. MeolaC (ed) (2012) Infrared thermography recent advances and future trends. Bentham eBooks, Sharjah
9. Holst GC (2000) Common sense approach to thermal imaging. SPIE Optical Engineering Press, Bellingham
10. Ibarra-Castanedo C, Tarpani J-R, Maldague XP (2013) Nondestructive testing with thermography. *Eur J Phys* 34:S91–S109
11. Ibarra-Castanedo C, Genest M, Piau J-M, Guibert S., Bendada A, Maldague XPV (2007) Chapter 16: active infrared thermography techniques for the nondestructive testing of materials. In: Chen CH (ed) Ultrasonic and advanced methods for nondestructive testing and material characterization, World Scientific Publishing, Singapore, 684p
12. Favro LD, Han X, Ouyang Z, Sun G, Sui H, Thomas RL (2000) Infrared imaging of defects heated by a sonic pulse. *Rev Sci Instrum* 71(6):2418–2421
13. Shepard SM, Ahmed T, Lhota JR (2004) Experimental considerations in vibrothermography. In: Burleigh DD, Cramer KE, Peacock GR (eds) Proceedings of SPIE—the international society for optical engineering, vol 5405. Thermosense XXVI, Orlando, pp 332–335

14. Zweschper T, Riegert G, Dillenz A, Busse G (2005) Ultrasound excited thermography—advances due to frequency modulated elastic waves. *J. QIRT* 2(1):65–76
15. Riegert G, Zweschper T, Busse G (2004) Lock-in thermography with eddy-current excitation. *J. QIRT* 1(1):21–32
16. Grenier M, Ibarra-Castanedo C, Luneau F, Bendada H, Maldague X (2002) Development of a field concentrator coil by finite element modeling for power efficiency optimization in eddy current thermography inspection. In: Thompson DO, Chimenti DE (eds) *Review of quantitative nondestructive evaluation vol 21*, pp 3–13
17. Lopez F, Nicolau V, Maldague X, Ibarra-Castanedo C (2013) Multivariate infrared signal processing by partial least-squares thermography. In: *international symposium on applied electromagnetics and mechanics*. Québec City, Canada, 31 July 2013–2 Aug 2013
18. Rajic N (2002) Principal component thermography, DSTO-TR-1298, <http://www.dsto.defence.gov.au/publications/2452/DSTO-TR-1298.pdf>. Accessed on 19 Dec 2013
19. Madruga FJ, Ibarra-Castanedo C, Conde OM, Lopez-Higuera J, Maldague X (2010) Infrared thermography based on higher-order statistics. *NDT&E Int* 43(8):661–666
20. Sfarra S, Ibarra-Castanedo C, Santulli C, Sarasini F, Ambrosini D, Paoletti D, Maldague X (2013) Eco-friendly laminates: from the indentation to non-destructive evaluation by optical and infrared monitoring techniques. *Strain* 49:175–189
21. Bendada A, Sfarra S, Genest M, Paoletti D, Rott S, Talmy E, Ibarra-Castanedo C, Maldague X (2013) How to reveal subsurface defects in Kevlar® composite materials after an impact loading using infrared vision and optical NDT techniques? *Eng Fract Mech* 108:195–208
22. Sfarra S, Bendada A, Paoletti A, Paoletti D, Ambrosini D, Ibarra-Castanedo C, Maldague X (2010) Square pulse thermography (SPT) and digital speckle photography (DSP): non-destructive testing (NDT) techniques applied to the defects detection in aerospace materials. In: *International symposium on NDT in aerospace*, Hamburg, Germany, 22–24 Nov 2010. Available online: <http://www.ndt.net/article/aero2010/papers/p3.pdf>
23. Rajic N (2002) Principal component thermography for flaw contrast enhancement and flaw depth characterization in composite structures. *Comp Struct* 58:521–528
24. Md. Akid H, De Rosa IM, Santulli C, Sarasini F (2010) Flexural behaviour of pultruded jute/glass and kenaf/glass hybrid composites monitored using acoustic emission. *Mat Sci Eng A-Struct* 527:2942–2950
25. Carmisciano S, De Rosa IM, Sarasini F, Tamburrano A, Valente M (2011) Basalt woven fibre reinforced vinylester composites: flexural and electrical properties. *Mater Design* 32(1):337–342
26. Sfarra S, Ibarra-Castanedo C, Santulli C, Paoletti A, Paoletti D, Sarasini F, Bendada A, Maldague X (2013) Falling weight impacted glass and basalt fibre woven composites inspected using non-destructive techniques. *Compos Part B-Eng* 45:601–608
27. Santulli C, Sarasini F, Tirillò J, Valente T, Valente M, Caruso AP, Infantino M, Nisini E, Minak G (2013) Mechanical behaviour of jute cloth/wool felts hybrid laminates. *Mater Design* 50:309–321

**Integrated Imaging and Vision Techniques for Industrial
Inspection**

Advances and Applications

Liu, Z.; Ukida, H.; Ramuhalli, P.; Niel, K. (Eds.)

2015, X, 541 p. 407 illus., 13 illus. in color., Hardcover

ISBN: 978-1-4471-6740-2